Compton Camera Arrangement With a Monolithic LaBr$_3$(Ce) Scintillator and Pixelated GAGG Detector for Medical Imaging

Silvia Liprandi, Sodai Takyu, Mohammad Safari, Tim Binder, George Dedes, Kei Kamada, Maria Kawula, Akram Mohammadi, *Member, IEEE*, Fumihiko Nishikido, Ingrid I. Valencia-Lozano, Rita Viegas, Taiga Yamaya, *Member, IEEE*, Katia Parodi, *Member, IEEE*, and Peter G. Thirolf

Abstract—The results presented in this manuscript are divided in two main parts. The aim of the presented work is to conduct feasibility tests on a Compton camera setup to be later scaled up and used for PET and triple coincidence γ-PET purposes. The first part is focused on laboratory characterization of a monolithic LaBr$_3$(Ce) scintillator coupled to a 64-channel multianode photomultiplier (H8500C PMT from Hamamatsu) in combination with a well-established algorithm allowing to determine the interaction's position resolution. The second part of the article is dedicated to the evaluation of a Compton camera detector arrangement in which the monolithic scintillator acts as an absorber, while a pixelated GAGG scintillator array, read out by a SiPM multipixel photon counter (MPPC), is used as a scatterer component. The accuracy achievable with this system for detecting γ rays from laboratory point sources is investigated. The Compton camera system has been tested with radioactive ^{137}Cs and ^{60}Co point sources. The signal readout and data acquisition system is based on individual spectroscopy electronics modules (NIM and VME), for the absorber and a customized electronics based on Anger logic for the GAGG scatter array. The raw data were analyzed to serve as input for the image reconstruction, performed using the MEGAlib toolkit software. With a spatial resolution of 1 mm for the scatterer and less than 3 mm for the absorber component, respectively, shifts of 2 mm of both radioactive sources (^{137}Cs and ^{60}Co) could be resolved with the whole Compton camera system.

Index Terms—γ-PET, Compton camera, hadron-therapy, monolithic scintillator, spatial resolution, triple-γ detection.

I. INTRODUCTION

POSITRON emission tomography (PET) is a widely investigated technique for medical imaging. An image is reconstructed from the two (almost) back-to-back emitted 511-keV β^+ annihilation photons and, depending on the PET isotope being used, the retrieved information can be used for either tumor diagnosis or range monitoring during tumor treatment. The emission of a third photon from the de-excitation of an excited β^+ daughter nucleus allows for the detection of a triple coincidence (the timing depends on the third gamma, which can be prompt or delayed). The determination of the trajectory intersection is then obtained between the prompt photon's trajectory and the line of response (LOR) from the β^+ decay of the PET isotope. By exploiting this coincidence, the so-called γ-PET (or whole gamma imaging [1]) technique aims at improving the sensitivity of the reconstructed image with a reduced requirement of reconstructed intersections per voxel compared to a conventional PET reconstruction analysis [2]. The resulting additional photon emission per individual β decay, instead of bringing an extra dose to the patient and a background enhancement for the PET signal, is, therefore, turned into an advantage by making use of the information carried by the third promptly emitted photon [1], [3].

Table I lists β^+-γ emitting isotopes suitable to be used with the γ-PET technique and as such applicable for tumor diagnosis in nuclear medicine or for range monitoring in radiation therapy. The half-life ($T_{1/2}$) of the β decay is indicated, together with the energy (E_γ) of the third photon, promptly emitted from the daughter nuclei of the β^+ decay.

Given the increasing impact of tumor illnesses nowadays, there is a great interest worldwide in investing for the improvement of their diagnosis and treatment techniques. The work carried out and presented in this article is intended to be a preparatory study for a future application as a γ-PET system for tumor diagnosis or beam range monitoring in hadron therapy. A full detector system could be composed of several

TABLE I
γ-PET Isotopes. The Half-Life ($T_{1/2}$) of the β^+ Decay and the Energy (E_γ) of the Third Photon, Promptly Emitted From the Daughter Nuclei, Are Indicated

Purpose	Isotope	$T_{1/2}$	E_γ
Tumour diagnosis	^{44}Sc	3.97 h	1157 keV
Ion beam range monitoring	^{10}C	19.10 s	718 keV
	^{14}O	70.60 s	2313 keV

TABLE II
Properties of GAGG [13] and LaBr$_3$(Ce) [14] Scintillation Crystals

Crystal	GAGG	LaBr$_3$(Ce)
Decay time [ns]	92	16
Light output [ph / MeV]	~ 56000	~ 63000
Emission wavelength [nm]	520	380
Density [g / cm^3]	6.63	5.08
Internal radioactivity	no	yes
Hygroscopic	no	yes

Compton camera arms for signal detection. Compton imaging is one of the techniques proposed and being investigated nowadays by different groups worldwide [4], [5], [6], [7], [8], [9], [10]: a Compton camera is composed of at least a scatterer and an absorber detector. From the energy and position information retrieved from the two components and using the Compton kinematics, a so called *Compton cone* can be reconstructed for each detected photon. When aiming at detecting a triple coincidence, this Compton cone can be intersected with the LOR from the PET signal. For the study presented here, a setup consisting of a single Compton camera arm has been evaluated, with the purpose of determining the achievable accuracy in the energy range and geometrical configuration of interest for nuclear medicine.

This setup is specifically suited to optimize the efficiency by adapting to photon energies below ca. 2 MeV, which is typical for the γ-PET mode (given the two 511-keV photons from the β^+ decay and the third promptly emitted photon from the daughter nuclei in Table I). This is in contrast to prompt gamma imaging, which could be studied alternatively during particle therapy, however, aiming at detecting much higher-(multi-MeV) photon energies [11]. In this scenario also Compton electron tracking could be performed in a suitable Compton camera configuration [12], which is deliberately excluded for the camera setup presented here.

II. MATERIAL AND METHODS

In this study, the investigated Compton camera setup was composed of a pixelated GAGG (Gd$_3$Al$_2$Ga$_3$O$_{12}$(Ce)) detector array as scatterer and a monolithic LaBr$_3$(Ce) scintillator as absorber. Table II summarizes the properties of both scintillation materials.

In Figs. 1 and 2 the structure (a) and the photographs (b) of the scatterer and absorber components are shown, respectively. The scatterer is formed by a segmented detector array and consists of 22 $\times$ 22 individual GAGG (Gd$_3$Al$_2$Ga$_3$O$_{12}$(Ce)) crystals, each of them with a size of 0.9 $\times$ 0.9 $\times$ 6 mm^3, optically separated by thin layers of BaSO$_4$ and wrapped together using 0.1-mm thick Teflon foils. For signal readout the array is coupled, as shown in Fig. 1, to an (8 $\times$ 8)
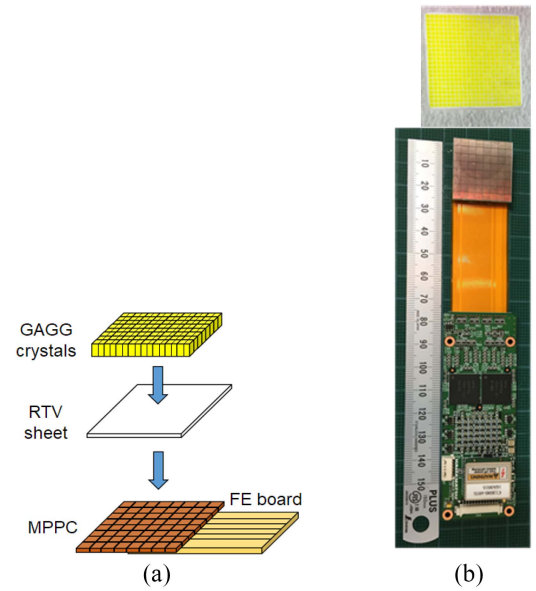

Fig. 1. (a) Sketch of the structure of the detector array used as Compton camera scatterer component: an array of 22 $\times$ 22 GAGG crystals is read out by an MPPC SiPM array (total area 25.8 $\times$ 25.8 mm^2) [16] with an RTV sheet placed in between for light guidance. (b) Photograph of the GAGG crystal array (top) read out by the MPPC SiPM array (bottom), connected to its customized frontend readout board developed by Hamamatsu Photonics [17].
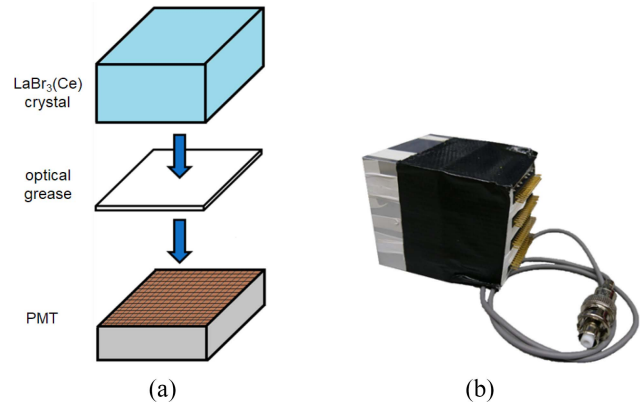

Fig. 2. (a) Sketch of the structure of the detector used as Compton camera absorber component: a monolithic LaBr$_3$(Ce) scintillation crystal (total area 50.8 $\times$ 50.8 mm^2) coupled to a 64-channel PMT (H8500C from Hamamatsu Photonics [18]) with a thin layer (<1 mm) of optical grease placed in between as light guide coupling. (b) Photograph of the detector.

segmented multipixel photon counter (MPPC) silicon photomultiplier (SiPM) array via an room temperature vulcanizing (RTV) light guide sheet (Shin-Etsu Chemical, KE420 [15]). The thickness of the RTV sheet was optimized from initially 0.1 mm [19] to 2 mm, respectively. The adjustment of the light guide between the scintillator and the SiPM as a way to suppress the SiPM saturation effect improved the energy resolution from 11% to 9.1% [20].

The signals were read out by an MPPC SiPM array with 8 $\times$ 8 channels, each 3 $\times$ 3 mm^2 (Hamamatsu S13361-3050AE-08: total area 25.8 $\times$ 25.8 mm^2, 3584 microcells/ch, microcell size = 50 μm [16]). The frontend signal processing of the 64-channel GAGG array was performed with

customized electronics from Hamamatsu Photonics [17], providing four output signals derived from a resistor network plus an additional sum signal, thus, enabling an Anger logic calculation for the photon interaction position determination, as given by (1). Here, X and Y are the interaction coordinates to be calculated in the coordinate system of the camera setup and A, B, C, and D are the four output signals from the resistor network [22]

$$X = \frac{-(A + C) + (B + D)}{A + B + C + D}; \quad Y = \frac{-(A + B) + (C + D)}{A + B + C + D}. \tag{1}$$

The material of the monolithic LaBr$_3$(Ce) absorber detector was chosen due to its excellent energy, time, and spatial resolution [23], the latter discussed in detail in the next section. When selecting the detector's configuration, two readout scenarios were actually taken into account. In the first one, which was then selected for the Compton camera setup configuration, the scintillator was read out by a segmented multianode photomultiplier (H8500C PMT from Hamamatsu [18]). In the second scenario, which in Section III-A will be called "via software from 16 × 16 PMT," the data originate from a reference library acquired using a 16 × 16 fold segmented PMT (Hamamatsu H9500). The available dataset is then reduced from 256 channels to 64 channels by applying a 2 × 2 software binning of neighbor pixels. The two scenarios were considered as their comparative spatial resolution performance at ^{60}Co energies still had to be demonstrated.

The coupling between crystal and photosensor was achieved using an optical grease (BC-630 [24]), placed as thin lightguide layer inbetween the two components. Fig. 2(b) shows a photograph of the LaBr$_3$(Ce) crystal coupled to the H8500C PMT. The scintillation crystal is housed in an aluminum encapsulation due to its hygroscopicity (see Table II).

A. Procedure to Determine the Interaction Position and Spatial Resolution of the Monolithic Scintillator

The photon interaction position inside the monolithic LaBr$_3$(Ce) and its spatial resolution were determined by using the k-nearest neighbors (k-NN) algorithm, in particular its CAP (Categorical Average Pattern) version [25]. The idea of the algorithm is based on the comparison of each photon event with a look-up table (LUT) (in our case composed of 4×10^6 events) with known interaction positions, in order to identify the most similar ones and, thus, retrieve the corresponding position information. While in its standard form the k-NN algorithm relies on comparing a specific photon response with all entries of the 2-D reference library to identify the k best matches, in the CAP version this comparison is performed individually for each irradiation position. The photon event to be compared to the LUT can be a known or an unknown event: in the first case the aim is to determine the spatial resolution, whereas in the second case the aim is to determine the actual unknown photon interaction position.

The events contained in the LUT form a 2-D light amplitude reference library, which is acquired beforehand via a response characterization measurement. A sketch of the setup for this measurement is shown in Fig. 3.
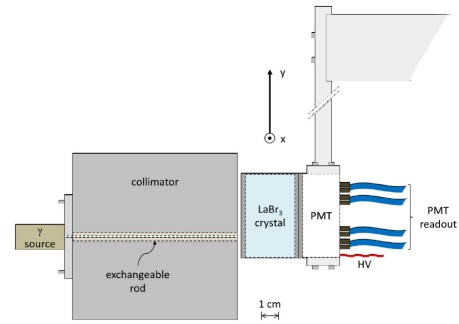

Fig. 3. Schematic setup for the 2-D detector scan measurement. A 2-D light amplitude reference library is created as LUT for the monolithic LaBr$_3$(Ce) scintillator.

Intense γ-ray calibration point sources (either ^{137}Cs with a photopeak energy of 662 keV or ^{60}Co with photopeak energies of 1173 and 1332 keV, respectively) are tightly collimated by placing them behind a $10 \times 10 \times 10$ cm^3 Densimet block (a high-density tungsten alloy) with a central 4-mm wide bore that carries an exchangeable tungsten carbide (WC) tube that defines the 1-mm collimator aperture. In addition, the source and the collimator block are surrounded by lead bricks to shield the detector surface from ambient background and enhance the contrast of the collimation by preventing sideways leakage of radiation. The monolithic LaBr$_3$(Ce) scintillator ($50.8 \times 50.8 \times 30$ mm^3) is mounted to a motorized 2-D translation stage and is placed directly in front of the collimator opening. A scan of the detector surface is performed in x and y directions with a step size of 0.5 mm [26]. For each of the 100×100 irradiation positions 400 photopeak events were acquired and saved to create the response reference library for the absorber detector. In order to obtain a reliable light amplitude distribution, where the maximum of the intensity reflects the actual spatial correlation between the irradiation position of the collimated γ source and the front surface of the scintillation detector, correction steps were applied to the raw data, which are briefly outlined here. Details on the correction procedure can be found in [12].

1) *Electronics Gain Matching:* In order to equalize the electronic amplifier gains for the individual signal channels, electronic pulser signals of different amplitudes were sent to the amplifier modules connected to each PMT channel (see also Fig. 5), allowing to determine individual gain and offset values.

2) *Pedestal Correction:* Since the contribution of the dark current (originating mainly from the QDC charge digitizer modules) may vary from channel to channel, a dedicated dark current measurement is performed for every electronic channel to allow applying a precise individual energy threshold to the recorded signals of each channel.

3) *PMT Nonuniformity Correction:* In order to take into account the gain fluctuations between the multianode PMT segments, the 2-D nonuniformity matrix provided by the manufacturer has to be considered. This matrix is unique for every PMT and contains the relative PMT segment gain factors for all the anode segments.
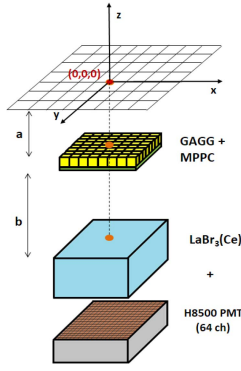
Fig. 4. Sketch of the Compton camera setup: The GAGG and LaBr$_3$(Ce) scintillation detectors (with an active front face area of 25.8×25.8 mm^2 and 50.8×50.8 mm^2, respectively) were placed in a relative distance of 50 mm, while the gamma source was placed in a distance of 45 mm from the scatterer component. Four different source positions in the (x, y) plane were investigated.

4) *Spatial Homogeneity Correction:* This step takes into account scattering and reflections inside the detector volume (predominantly at the edges and corners) by exploiting the internal radioactivity of LaBr$_3$(Ce), assumed to be homogeneously distributed in the detector volume, thus, producing an isotropic emission. The response of all different PMT segments is then used to correct the light distribution data for spatial inhomogeneities of the crystal response.

5) *Photopeak Gating Correction:* Finally, a software energy gate is applied to the acquired data, corresponding to the region of interest for the specific photon source, i.e., selecting the photopeak energy of the collimated source.

The uncertainties for the spatial resolution values were calculated based on statistical uncertainties derived from sub-samples of the complete acquired reference libraries. From the total number of photopeak events collected per irradiation position (n_{epp}) sublibraries were created, each containing 100 events per position. The CAP algorithm was then applied to each sublibrary in order to derive a spatial resolution value for each of them. The standard deviation emerging from the distribution of the individual sublibrary results is then assigned as the experimental uncertainty of the full-library spatial resolution.

B. Compton Camera Configuration

In this study, a Compton camera setup was characterized in view of its possible γ-PET application in nuclear medicine [3]. The Compton camera setup was assembled with the detector components presented before: a pixelated GAGG (Gd$_3$Al$_2$Ga$_3$O$_{12}$(Ce)) detector array as a scatterer and a monolithic LaBr$_3$(Ce) as absorber. The Compton camera was investigated at different photon energies: $E_\gamma = 662$ keV from a ^{137}Cs point source and both $E_\gamma = 1173$ keV and $E_\gamma = 1332$ keV from a ^{60}Co point source. The Compton camera performance was evaluated in the geometrical configuration shown in Fig. 4, where the distances between the detector components and the source are commensurate to a possible future γ-PET scenario.
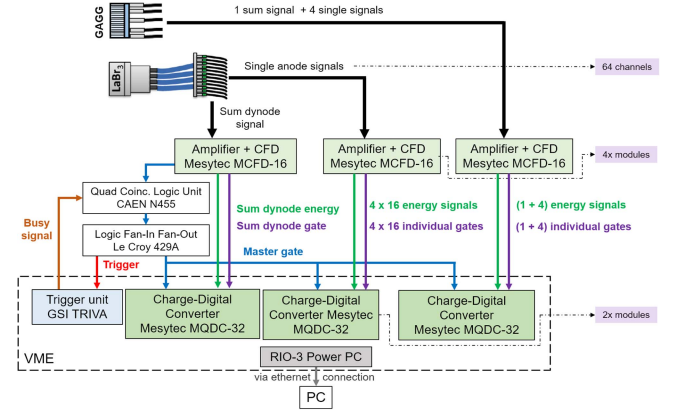

Fig. 5. Block diagram of the signal processing and data acquisition chain for the Compton camera system composed of a pixelated GAGG array and a monolithic LaBr$_3$(Ce) detector. The GAGG scatter detector provides a sum signal and four additional signals, used for an Anger-logic position calculation. The 64 individual signals from the LaBr$_3$(Ce) detector are read out together with its sum dynode signal, which is also used as a trigger signal for the whole system. All signals were processed by MCFD-16 [27] NIM modules and MQDC-32 [28] VME modules.

The two detectors were placed at a relative distance of 50 mm ((b) in Fig. 4), whereas the source plane was 45 mm away from the scatter detector front surface (distance (a) in Fig. 4). In order to evaluate the performance of this Compton camera detector configuration, four different lateral source positions were chosen, both for the ^{137}Cs and the ^{60}Co radioactive sources. The sources were sequentially placed in the following (x, y) positions: (0,0), (2,2), (4,4), (8,8) mm and data were acquired and analyzed for each of these positions.

In Fig. 5 a block diagram of the signal processing and data acquisition chain for the Compton camera system under study is sketched. The four output signals generated by the resistor network attached to the MPPC readout of the pixelated GAGG crystal array are first preamplified in a customized frontend board from Hamamatsu before being sent in parallel to different channels of an MFDC (NIM-)module (MCFD-32 from Mesytec [27]), for an amplification of the analog signal and generation of logic state signals in a constant fraction discriminator (CFD) stage. The frontend generated sum signal from the scatter array carrying the information acquired from the whole detector volume is also sent to a separate channel of an MCFD module. For all five signals this signal processing stage is followed by the integration and digitization of the collected electrical charge in an MQDC charge-to-digital converter VME module (MQDC-32 from Mesytec [28]).

The LaBr$_3$(Ce) absorber detector provides 64 individual signal channels, corresponding to the PMT segmentation, and a sum dynode signal, given by the total electrical charge collected at the last dynode of all the PMT pixels. All these (64 + 1) signals are processed by individual channels of MCFD (amplifier + CFD) modules followed by MQDC digitizer modules. In order to synchronize the data being recorded from both the scatterer and the absorber detectors, the sum signal from the LaBr$_3$(Ce) detector served as trigger for the whole Compton camera system. Fig. 5 indicates the electronic stages needed to create the trigger signal. A logic signal was

created by a dedicated MCFD module receiving the absorber PMT sum dynode signal as input. This signal was then sent to a logic unit (Quad. Coinc. Logic Unit, CAEN N455 [29]) and a logic fan-in fan-out module (Le Croy 429A [30]) in order to generate both the trigger signal and the master gates. The latter ones were sent to each MQDC module to synchronize the start of the charge integration in each channel. The trigger was controlled by a trigger unit (TRIVA from GSI [31]), which was communicating with the logic unit sending a busy signal to the logic branch to prevent the processing of events while the acquisition chain was still busy. The trigger signal was also connected via the VME bus to all MQDC modules and to a PowerPC (RIO-3 PowerPC [32]) frontend CPU, running the data acquisition system Marabou under the realtime operation system LynxOS [33]. Finally, the RIO-3 PowerPC sent the acquired data to a remote computer station for online analysis and storage.

C. Data Analysis

The central data analysis goal was to reconstruct the image of the radioactive point source placed at different positions, to gain insight into the Compton imaging performance in controlled scenarios. This reconstruction is based on the intersection of Compton cones defined by the position and energy information of both detector components of the camera. These data were provided as input for the MEGAlib software toolkit [34], which is based on the list-mode maximum-likelihood expectation-maximization (LM-ML-EM) algorithm [35]. This toolkit was used as well for generating simulated data used for benchmarking the experimental results. Since the detailed procedures to obtain the simulated data and to perform the image reconstruction are beyond the scope of this article, only the key input parameters to MEGAlib will be presented together with the results in comparison to the experimental data, which in turn will be presented in detail. The reconstructed images obtained from both simulated and experimental data were quantitatively analyzed via a fit based on a 2-D Gaussian model. The results are presented in the next section, while the following section describes the analysis steps followed to prepare the scatterer and absorber data for the image reconstruction. Since the data were acquired in coincidence between the two camera components (using the sum signal from the absorber as trigger for the whole system as indicated in Fig. 5), for each of the recorded events energy and position information can be extracted from both detectors and accordingly conditioned to derive energy and spatial information from Compton scattering events. The different analysis steps applied to the raw data are summarized in the following list.

1) *Accumulate 2-D Energy Plot:* For each measurement with the Compton camera a 2-D plot was created, containing the information from the total energy deposited in the absorber component versus the total energy registered in the scatterer component. At this analysis step the total number of triggering and acquired events is still preserved. Examples of such plots are shown in Figs. 6 and 7 together with the description of the
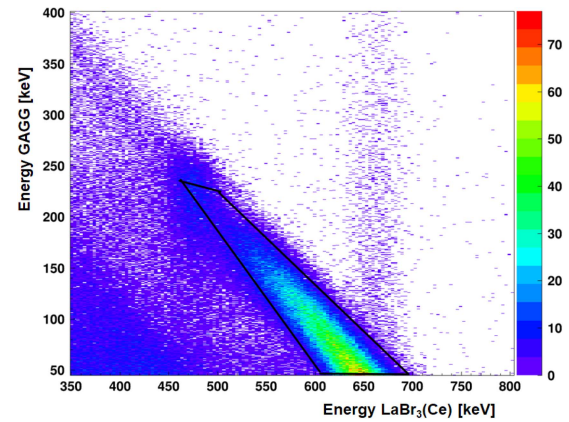

Fig. 6. 2-D energy correlation between the total energy registered in the Compton camera absorber component (serving as trigger for the data acquisition, plotted along the *x*-axis) and in the scatter component, as represented by the *y*-axis. Events in Compton-scattering coincidence are located within the area encircled by the black polygon. This figure refers to the geometrical configuration where scatterer and absorber had a relative distance of 50 mm and a ^{137}Cs point source was placed in a distance of 45 mm from the scatterer front surface at the (0,0,0)-mm position.
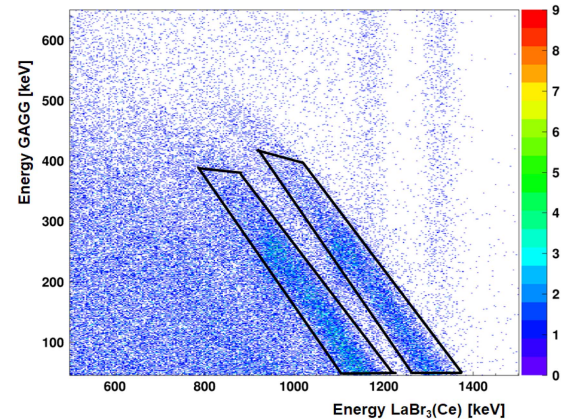

Fig. 7. 2-D energy correlation between the total energy registered in the Compton camera absorber component (serving as trigger for the data acquisition, plotted along the *x*-axis) and in the scatter component, as represented by the *y*-axis. Events in Compton-scattering coincidence are located within the area encircled by the two black polygons. This figure refers to the geometrical configuration where scatterer and absorber had a relative distance of 50 mm and a ^{60}Co point source was placed in a distance of 45 mm from the scatterer at the (0,0,0)-mm position.

2-D energy cut applied to select Compton-scattered coincidence events.

2) *Select Coincidence Events:* A 2-D energy cut is applied to the energy correlation between absorber and scatterer, selecting events around the diagonal region representing the photopeak energy of the γ source. The width of the cut is adjusted according to the energy resolution of the triggering detector. In Figs. 6 and 7 the 2-D energy correlation plot and the correspondingly applied 2-D energy cut are shown for the case of the ^{137}Cs and ^{60}Co sources, respectively. In Fig. 6 a 2-D cut is applied around the ^{137}Cs photopeak energy at 662 keV, while in Fig. 7 two cuts are applied for the ^{60}Co photopeak energies of 1173 and 1332 keV, respectively. Applying these cuts removes most of the random coincidences.
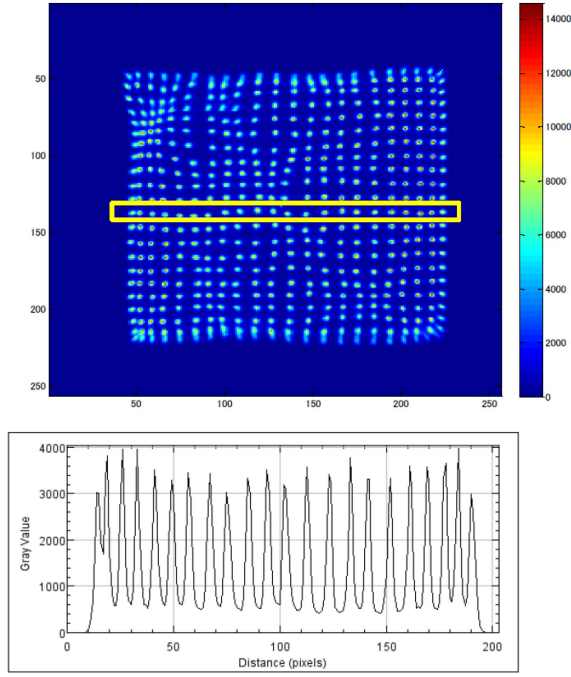
Fig. 8. Flood map of the (22 × 22) pixelated GAGG detector, used as LUT. The x-axis projection of the pixel positions for the pixel row specified by the yellow rectangle is also shown. The map was obtained using a ^{22}Na point source [21].

3) *Write Coincidence Events in ASCII Files:* For each detector a text file is created under the filtering condition applied during the previous analysis step. It contains the energy amplitude values registered in each electronic channel for each coincidence event. The same ordering of events is preserved in both detector files, in order to maintain the event synchronization.

4) *Reconstruction of the Photon Interaction Position:* The ASCII files created in the previous analysis step are used as inputs for the algorithms that serve to reconstruct the photon interaction positions in the two detector components: a) Anger-logic calculation and b) k-NN algorithm for scatterer and absorber component, respectively. The scintillation light amplitude data from the individual PMT segments of the LaBr₃(Ce) crystal were compared to the reference library that was created as described in Section II-A applying the CAP algorithm. For the pixelated GAGG scatterer component the four output signals allowed for the (x, y) photon interaction position to be calculated using an Anger-logic method [as given by (1)]. The obtained positions were then compared to a LUT to derive the precise x and y coordinates of the specific responding crystal within the GAGG array. The flood map of the (22 × 22) pixelated GAGG detector used as LUT is depicted in Fig. 8. The upper part of the figure shows the 2-D flood map. Additionally, in the bottom part the x-axis projection of the pixel positions is shown for the pixel row specified by the yellow rectangle. The LUT for this study was obtained with a specific calibration run using a ^{22}Na calibration point source, which was placed in front of the scatter detector. Data

were acquired using its sum signal as trigger. This source was selected because of its two photopeaks located at positions in the energy spectrum relevant for our purpose: both 511 and 1275 keV are energies of interest for γ-PET Compton imaging. Since a depth-of-interaction (DOI) correction capability for these detectors was not available, the z coordinate of the interaction position was set to lie on the (x, y) middle plane of the detectors (considering the 6 and 30-mm thickness of the GAGG and LaBr₃(Ce) crystals, respectively).

5) *Removing Nonphysical Scattering Angles:* From the validated set of coincident events, those exhibiting unphysical scattering angles were discarded by applying the kinematical relation

$$\cos\theta = 1 - m_e c^2 \left(\frac{1}{E_{\mathrm{abs}} - \frac{1}{E_{\mathrm{abs}} + E_{\mathrm{scatt}}}} \right) \quad (2)$$

where E_{abs} and E_{scatt} represent the energies deposited in the absorber and scatter components, respectively, θ is the Compton scattering angle of the incident gamma ray and m_e is the electron mass. The following selection condition was applied to retain only events with physically meaningful scattering angles:

$$0 < m_e c^2 \left(\frac{1}{E_{\mathrm{abs}} - \frac{1}{E_{\mathrm{abs}} + E_{\mathrm{scatt}}}} \right). \quad (3)$$

6) *ASCII Files Creation for MEGAlib:* From the events which survive all selection criteria listed in the above analysis steps, an ASCII file was created as input for the MEGAlib software toolkit: it contains, for each identified and validated Compton scattering event, the position and energy information from each of the two detector components of the Compton camera system.

Once the energy and position information were retrieved for each of the two detector components and for each of the coincident Compton-scattering events, the source image could be reconstructed using MEGAlib.

Subsequently, each of the reconstructed images was fitted using a 2-D Gaussian function in order to obtain the (x, y) centroid as the calculated source position. The nominal source position was then subtracted from the calculated coordinates to retrieve the resulting Δx and Δy deviation values in both directions as a measure for the accuracy of the applied method. From the 2-D Gaussian fit the standard deviations σ_x and σ_y of the centroid position were also derived, in order to quantify the precision of the imaging capabilities of this Compton camera setup.

The angular resolution measurement (ARM), defined as the width of the Compton cone reconstructed from each photon event, was also calculated for the photon energies of interest. It will be exemplary presented only for the configurations in which the source was placed in the central position, since the ARM is affected mostly by the fixed relative distance between the detector components, rather than by the source position in the (x, y) plane. A sketch explaining the concept of the ARM is shown in Fig. 9.
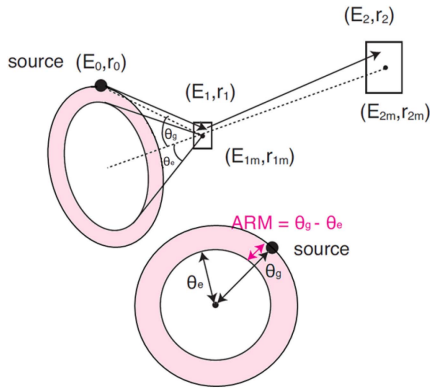
Fig. 9. Schematical description of the ARM. A photon source located in position r_0 and emitting an energy E_0 deposits an energy E_{1m} at r_{1m} in the scatterer and the remaining energy E_{2m} at r_{2m} in the absorber. The ARM is defined as $\theta_g - \theta_e$ [36], where θ_g is calculated from the measured interaction positions and the true direction of the source and θ_e is calculated from the measured energy deposits.

Fig. 10. Spatial resolution of the monolithic LaBr$_3$(Ce) scintillator as a function of the photon energy. The data originate from 2-D light amplitude reference libraries acquired with a 1-mm collimator and a 0.5-mm scan pitch size. The horizontal red dashed line denotes the design goal of 3 mm from the initial simulation studies performed for the Compton camera prototype specification [2].

TABLE III
SPATIAL RESOLUTION VALUES (AVERAGED OVER THE FULL ACTIVE LABR$_3$(CE) FRONT SURFACE AREA) OBTAINED WITH THE CAP VERSION OF THE k-NN ALGORITHM

PMT granularity	Spatial resolution [mm]		
	662 keV	1173 keV	1332 keV
64 (via software from 16×16 PMT)	4.2(1)	3.0(1)	2.9(1)
64 (8×8 PMT)	3.4(1)	2.9(1)	2.9(1)

III. RESULTS

This section presents the results obtained in this study for the imaging capability of the presented two-layer Compton camera system. The section is divided in two main parts, the first one focusing on results related to the spatial resolution of the monolithic LaBr$_3$(Ce) scintillation crystal via the k-NN algorithm and the second one focuses on the characterization of the imaging capabilities of the Compton camera setup.

A. Spatial Resolution of the Monolithic Scintillator

This first section presents the outcome of an optimization of the well-established k-NN method for determining the spatial resolution of the monolithic LaBr$_3$(Ce) scintillator read out by a segmented PMT and serving as absorber component of the Compton camera under study.

In Table III a summary of the energy dependent spatial resolution achieved using the CAP version of the k-NN algorithm is given.

The spatial resolution obtained for three photon energies (662, 1173, and 1332 keV, respectively) is listed for two readout scenarios, which were introduced in Section II-A. For the case "via software from 16 × 16 PMT" the data initially originate from a 16 × 16 fold segmented PMT (Hamamatsu H9500) and were reduced during the data offline analysis to 64 signal channels by combining each adjacent quadruple of signals, whereas for the second data set ("8 × 8 PMT") the monolithic scintillator was directly coupled to an 8 × 8 fold segmented PMT (Hamamatsu H8500C).

Already in [26] it was demonstrated that a higher-PMT granularity does not provide better spatial resolution (reflecting the advantage of hi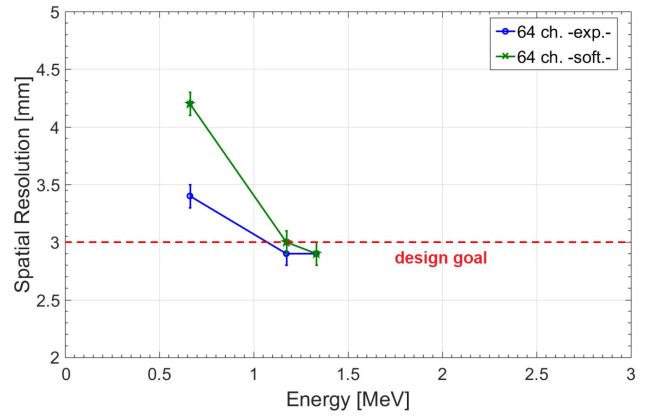gher-photon statistics collected in larger PMT segments). Together with the results obtained with the optimized version of the k-NN algorithm and listed in Table III, this motivates the choice of an 8 × 8 fold segmented PMT as photosensor for the Compton camera absorber crystal under study here. The values listed in Table III are also plotted in Fig. 10.

All data of the reference libraries (LUT) used for the CAP (k-NN) calculations were acquired with a setup [12] using the following characteristics: 1-mm collimation diameter and 0.5-mm scan pitch size. The parameters for the CAP algorithm were set to be $n_{epp} = 400$ (number of photopeak events collected per irradiation position) and kCAP = 12 (number of k best matching 2-D light amplitude distributions per irradiation position) [26], [37].

Starting from the lowest energy sat 662 keV, a trend of an improving spatial resolution with increasing photon energies can be observed. This translates as well to the overall resolution of the Compton camera, both in terms of the width of the reconstructed images expressed by the standard deviation σ and in terms of the angular resolution measure (ARM) (see Section III-B). The best value of 2.9(1) mm is reached, within uncertainties, for both ^{60}Co photopeak energies. This result can be understood by the fact that the two ^{60}Co photon energies are rather close to each other, making an appreciable difference of the spatial resolution rather unlikely. The less energetic 662-keV γ rays originating from the ^{137}Cs source are characterized by a shorter radiation length. Therefore, they tend to interact within the scintillation crystal further away from the PMT's entrance window: this increases the probability of scattering and attenuation of the scintillation light before being detected by the photosensor.

The uncertainties given for the spatial resolution in Table III and Fig. 10 were calculated based on statistical uncertainties derived from subsamples of the complete acquired reference libraries, as previously described in Section II-A.

B. Compton Camera Configuration

This section is dedicated to the results obtained for the Compton camera imaging properties. As previously described
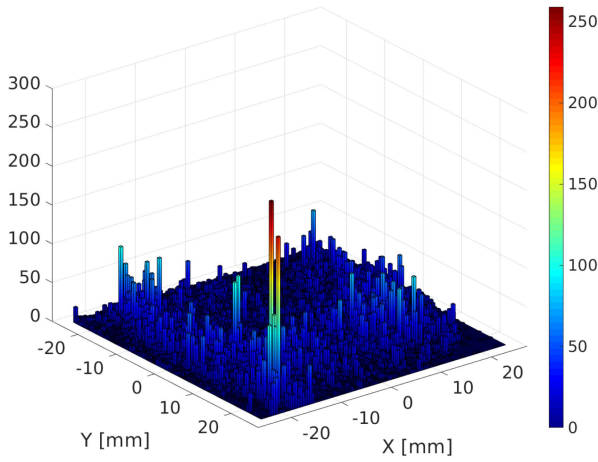
Fig. 11. Reconstructed photon interaction positions in the monolithic LaBr₃(Ce) scintillator crystal. The data of this plot were retrieved from events acquired in a geometrical arrangement in which scatterer and absorber had a relative distance of 50 mm and a ^{137}Cs source was placed in a distance of 45 mm from the scatterer at the (0,0,0)-mm position.

TABLE IV
RELATIVE ENERGY AND SPATIAL RESOLUTION OF THE TWO
COMPTON CAMERA CONSTITUENTS USED AS INPUT FOR
MONTE CARLO SIMULATIONS

		scatterer	absorber
Energy resolution	662 keV	9.1 %	3.8 %
	1173 keV	6.9 %	3.2 %
	1332 keV	6.4 %	2.7 %
Spatial resolution	662 keV	1.0 mm	3.4(1) mm
	1173 keV	1.0 mm	2.9(1) mm
	1332 keV	1.0 mm	2.9(1) mm

in Section II-C, for the characterization measurements performed with this system, the events were acquired using the LaBr₃(Ce) sum dynode signal as trigger. Only Compton scattered events acquired in coincidence between scatterer and absorber were selected for the subsequent interaction position determination and source image reconstruction via a 2-D energy gate as illustrated in Figs. 6 and 7 (for impinging photons from ^{137}Cs and ^{60}Co sources, respectively).

For the studies using ^{137}Cs, from a total of around 1.6×10^7 triggered events, acquired in about 4 h, 1.7×10^5 events were filtered by the coincidence condition and the 2-D energy cut. During the ^{60}Co measurements around 9×10^6 events were initially triggered and acquired in about 6 h of measurement time. Finally, $\approx 2.3 \times 10^4$ and 1.5×10^4 events were extracted after the analysis conditions related to the photopeak energies of 1173 and 1332 keV, respectively. These numbers reflect the limited scattering probability of the GAGG array (decreasing with increasing photon energy), which, due to constraints in the signal processing electronics, could not be used as trigger during the data acquisition.

For each photon energy and each geometrical detector configuration under study, the data selected as part of the Compton kinematics calculation were separately analyzed to obtain the photon interaction position and energy deposition information from both components of the Compton camera (Section II-C): the data from the GAGG detector array were analyzed based on an Anger logic algorithm, while the position data from the LaBr₃(Ce) absorber were derived using the CAP version of the k-NN algorithm. ASCII files were created, containing for each identified coincident Compton event the photon interaction positions found in the two detectors and their corresponding photon energies.

In Fig. 11 an example of reconstructed interaction positions on the 2-D surface area of the monolithic scintillator is depicted. The data represent Compton events acquired in a geometrical arrangement where scatterer and absorber had a relative distance of 50 mm and a ^{137}Cs source was placed

in a distance of 45 mm from the scatterer at the (0,0,0)-mm position. It can be seen that the CAP (k-NN) algorithm reconstructs the photon interaction positions quite homogeneously distributed in the lateral parts of the surface area, whereas the interaction rate in the central area of the LaBr₃(Ce) surface area is higher, consistent with the central ^{137}Cs source position relative to both detectors.

Data were analyzed for all three photon energies of interest (662, 1173, and 1332 keV) and for various photon source positions according to the steps described in Section II-C. ASCII files were created as input for the MEGAlib toolkit [34] that was applied for the source image reconstruction.

A performance comparison was conducted between images reconstructed from both experimental and simulated data.

Energy and spatial resolution values of the Compton camera scatterer and the absorber components are listed in Table IV. These properties were used as input for Monte Carlo simulations performed to generate simulated data sets for different source positions (Section II-B), finally allowing for a comparison of simulated and experimental reconstructed source images.

In Fig. 12 the point source images reconstructed from simulated (left) and experimental (right) data from a ^{137}Cs source are depicted for four different source positions. All images were acquired for a relative distance between scatterer and absorber along the z-axis of 50 mm, while the ^{137}Cs source was placed at a distance of 45 mm from the scatterer's front surface. Four different γ-source positions in the (x, y) plane were selected: (0,0), (2,2), (4,4), and (8,8) mm.

For each of the reconstructed images, a white cross hair is included to indicate the true source position. The intensity maxima in all reconstructed images were normalized to one for better comparison.

Comparing the source images reconstructed from simulated and experimental data, it can be seen that the source position is reasonably well reconstructed for both simulated and experimental data. The higher noise present in the images reconstructed from experimental data deserves a comment: it is mostly due to scintillation light scattering inside the detectors and this effect is not visible in the same way in the images reconstructed from simulated data since the simulation itself did not include optical photon propagation.

Aiming for a quantitative analysis, as outlined in Section II-C, the reconstructed images were analyzed by applying a 2-D Gaussian fit: calculated (x, y) centroid source positions can be derived for each image. The true source position was then subtracted from the calculated one and the
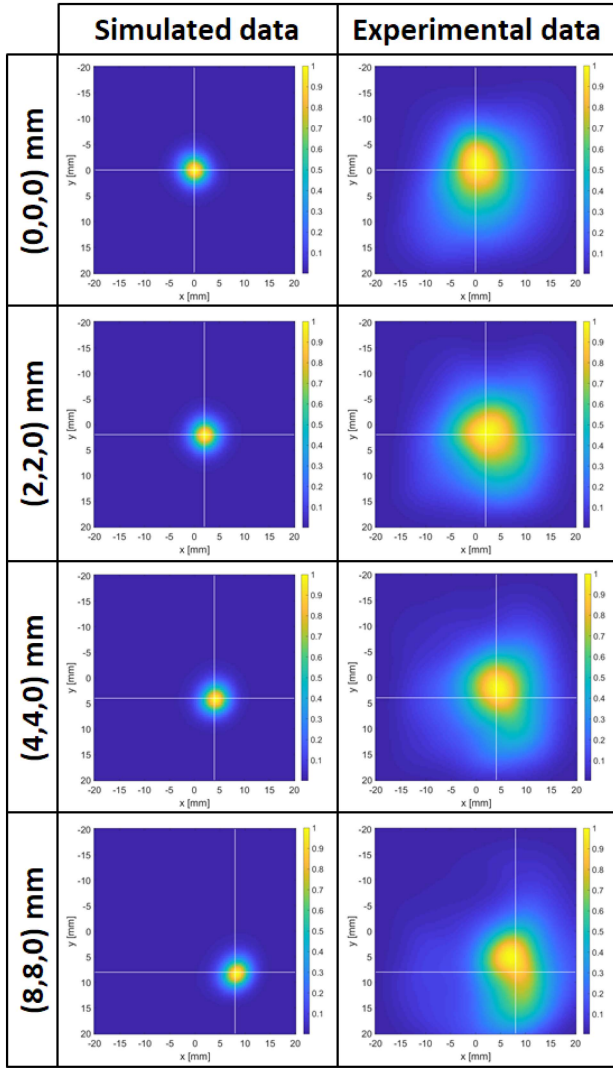
Fig. 12. Reconstructed ^{137}Cs source position from simulated data (left column) and experimental data (right column). The images refer to a geometrical arrangement in which scatterer and absorber had a relative distance of 50 mm and a ^{137}Cs source was placed in a distance of 45 mm from the scatterer's front surface at positions located at (0,0,0), (2,2,0), (4,4,0), and (8,8,0) mm according to the coordinate system introduced in Fig. 4 and indicated by the white cross hairs.

resulting Δx and Δy values were obtained, as compiled in Table V, and found to indicate deviations from the true source positions of <1.5 mm.

The width of the reconstructed image as expressed by the standard deviation σ in the x and y direction was found to be between a value of 2 and 3 mm for the reconstructed images from simulated data and between 5 and 10 mm for the images from experimental data.

The angular resolution measure ARM was determined to be 8° for images obtained from simulated data and about twice this amount for images from experimental data.

For the Compton camera characterization using the ^{60}Co source, Fig. 13 presents the corresponding reconstructed source position images. They illustrate the same four source positions already used with the ^{137}Cs source at z=0 and placed in the (x, y) plane at (0,0), (2,2), (4,4), and (8,8) mm. As before in Fig. 13 the white cross hairs indicate the true source positions. Comparing the reconstructed images

TABLE V
(Δ_x, Δ_y) CALCULATED FROM THE 2-D GAUSSIAN FIT OF THE RECONSTRUCTED ^{137}CS SOURCE IMAGES

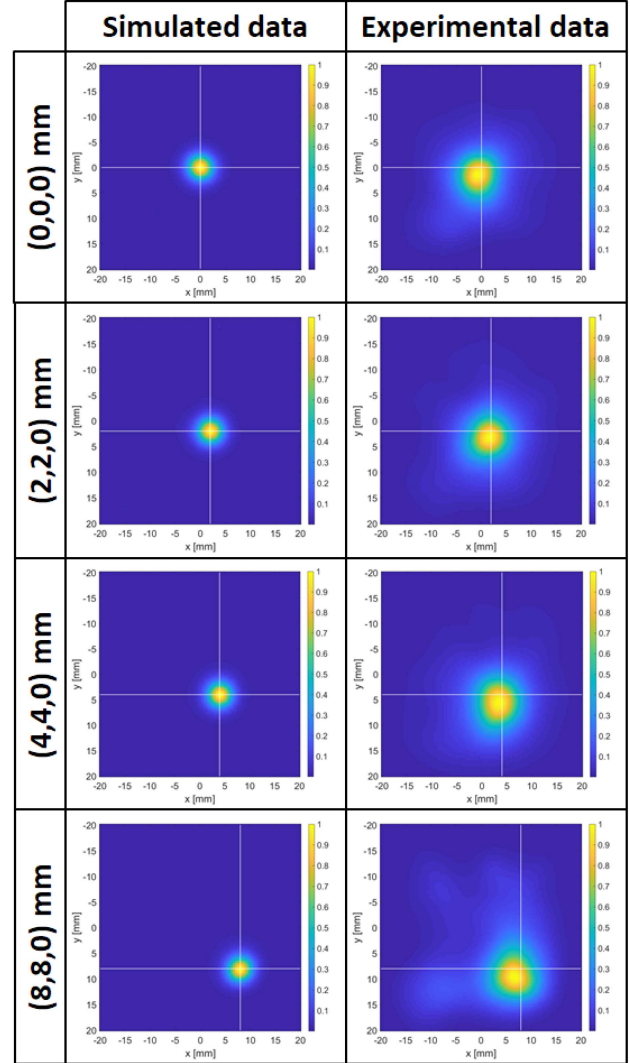| (x,y) source position [mm]	Δ_x [mm]		Δ_y [mm]	
	Sim	Exp	Sim	Exp
(0,0)	0.25	0.92	0.19	1.03
(2,2)	0.31	1.53	0.27	0.77
(4,4)	0.37	1.16	0.32	-0.64
(8,8)	0.33	-0.01	0.37	-0.04

Fig. 13. Reconstructed ^{60}Co source position from simulated data (left column) and experimental data (right column). The images refer to a geometrical arrangement in which scatterer and absorber had a relative distance of 50 mm and a ^{60}Co source was placed in a distance of 45 mm from the scatterer at positions located at (0,0,0), (2,2,0), (4,4,0), and (8,8,0) mm according to the coordinate system introduced in Fig. 4 and indicated by the white cross hairs.

from simulated and measured ^{60}Co data, in both cases the source position is again reasonably accurately reconstructed, which is quantitatively demonstrated by the Δx and Δy values listed in Table VI. Again the higher noise in the experimental reconstructed images is visible.

Following again the data analysis procedure previously described, the images are fitted using a 2-D Gaussian function and Δ_x and Δ_y values are derived as the difference between

(x,y) source position [mm]	Δ_x [mm]		Δ_y [mm]	
	Sim	Exp	Sim	Exp
(0,0)	0.24	-0.44	0.20	1.76
(2,2)	0.22	-0.2	0.16	-0.71
(4,4)	0.24	-0.54	0.19	1.68
(8,8)	0.10	-1.26	0.22	0.96

Fig. 14. Reconstructed image from ^{60}Co source placed in position (2,2,0) mm. The projections on the *x*- and *y*-axes of the image are shown as well, together with the Gaussian fit of each of the two projection curves.

the calculated and true (x, y) coordinates of the source. As in the case of the ^{137}Cs data, the statistical uncertainties of the (x, y) centroid fit are found to be negligible.

Table VI summarizes the resulting Δx and Δy values, found to indicate an agreement between reconstructed and true source positions of better than 1.8 mm.

The standard deviation σ in x and y direction was found to be 1.5–2.5 mm for the reconstructed images from simulated data and between 2 and 6 mm for the images from experimental data.

The ARM for the ^{60}Co source image reconstruction was found to be 6° for images obtained from simulated data and about twice this amount for images from experimental data, reflecting an expected improvement with respect to the results using a ^{137}Cs source because of the higher-initial photon energy and the correspondingly better spatial resolution of the absorber component. The smaller ARM directly relates to the smaller image widths as expressed by the σ values reported above.

In order to illustrate the 2-D Gaussian fit procedure applied to obtain the results presented above, Fig. 14 exemplarily shows the image reconstructed for the ^{60}Co source placed at (2,2,0) mm. On the left, the Gaussian fit applied to the image projected onto the *y*-axis is shown, whereas below the 2-D image the Gaussian fit applied to the image projected on the *x*-axis is depicted. The maximum of the image was normalized to one. The shape of the reconstructed source image is very well reproduced by the Gaussian fit. Only in the tails far from the centroid (equivalent to the source position) some scattering noise is visible, lower than in the ^{137}Cs source case thanks to the better absorber spatial resolution, while both centroid and width of the image distribution can reliably be inferred from the 2-D fit.

IV. DISCUSSION AND CONCLUSION

A study for a two-layer Compton camera setup composed of a pixelated GAGG array and a monolithic LaBr₃(Ce) scintillation crystal was performed. The Compton imaging capability was characterized at different photon energies from both a ^{137}Cs and a ^{60}Co radioactive point source. The images of the point sources, placed at different positions shifted by 2 mm in x and y directions on the xy plane, were reconstructed using the MEGAlib software toolkit, based on the LM-ML-EM algorithm. The results obtained from experimental data were compared to results obtained from data received from Monte Carlo benchmarking simulations, obtaining in both cases reasonably well reconstructed source positions. The simplification needed to generate simulated data explains
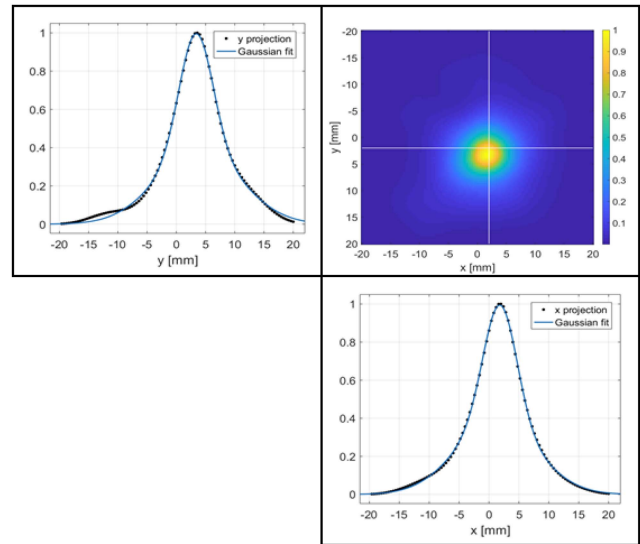
the higher-noise observable in the images reconstructed from experimental data. The scintillation light scattering inside the detectors, obviously present in the experimental data, was not comprised in the simulations since they did not include optical photon propagation. The spatial resolution for the monolithic absorber, obtained with the CAP algorithm and improving at higher energies, reflected in improved results for the whole Compton camera system at the highest energies considered.

Overall, it can be concluded that the presented feasibility study resulted in a satisfactory image reconstruction accuracy, allowing to identify source position shifts of 2 mm for both ^{137}Cs and ^{60}Co photopeak energies and marking a first step toward the applicability of the presented Compton imaging concept for γ-PET imaging in nuclear medicine as well as for range monitoring in hadron therapy.

ACKNOWLEDGMENT

REFERENCES

[1] E. Yoshida et al., "Whole gamma imaging: A new concept of PET combined with Compton imaging," *Phys. Med. Biol.*, vol. 65, no. 12, 2020, Art. no. 125013.

[2] C. Lang, D. Habs, K. Parodi, and P. G. Thirolf, "Sub-millimeter nuclear medical imaging with high sensitivity in positron emission tomography using beta-gamma coincidences," *J. Instrum.*, vol. 9, Jan. 2014, Art. no. P01008, doi: 10.1088/1748-0221/9/01/P01008.

[3] T. Yamaya et al., "Concrete realization of the whole gamma imaging concept," in *Proc. IEEE NSS-MIC Conf.*, 2017, pp. 1–3.

[4] S. Motomura, S. Enomoto, H. Haba, K. Igarashi, Y. Gono, and Y. Yano, "Gamma-ray Compton imaging of multitracer in biological samples using strip germanium telescope," *IEEE Trans. Nucl. Sci.*, vol. 54, no. 3, pp. 710–717, Jun. 2007.

[5] S. Kabuki et al., "Electron-tracking Compton gamma-ray camera for small animal and phantom imaging," *Nucl. Instrum. Methods Phys. Res. Sect. A, Accelerators Spectrometers Detectors Assoc. Equip.*, vol. 623, pp. 606–607, Nov. 2010.

[6] S. Takeda et al., "Demonstration of in-vivo multi-probe tracker based on a Si/CdTe semiconductor Compton camera," *IEEE Trans. Nucl. Sci.*, vol. 59, no. 1, pp. 70–76, Feb. 2012.

[7] A. Kishimoto et al., "First demonstration of multi-color 3-D *invivo* imaging using ultra-compact Compton camera," *Sci. Rep.*, vol. 7, p. 2110, May 2017.

[8] M. Sakai et al., "In vivo simultaneous imaging with ^{99m}Tc and ^{18}F using a Compton camera," *Phys. Med. Biol.*, vol. 63, Oct. 2018, Art. no. 205006.

[9] K. Shimazoe et al., "Development of simultaneous PET and Compton imaging using GAGG-SiPM based pixel detectors," *Nucl. Instrum. Methods Phys. Res. Sect. A, Accelerators Spectrometers Detectors Assoc. Equip.*, vol. 954, Feb. 2020, Art. no. 161499.

[10] T. Nakano et al., "Imaging of ^{99m}Tc-DMSA and ^{18}F-FDG in humans using a Si/CdTe Compton camera," *Phys. Med. Biol.*, vol. 65, no. 5, p. 5LT01, 2020.

[11] J. Krimmer, D. Dauvergne, J. M. Létang, É. Testa, H. Kopka, and P. W. Daly, "Prompt-gamma monitoring in hadrontherapy: A review," *Nucl. Instrum. Methods Phys. Res. Sect. A, Accelerators Spectrometers Detectors Assoc. Equip.*, vol. 878, pp. 58–73, Jan. 2018.

[12] S. Aldawood et al., "Development of a Compton camera for prompt-gamma medical imaging," *Radiat. Phys. Chem.*, vol. 140, pp. 190–197, Nov. 2017.

[13] "C&A corporation." Accessed: Sep. 2022. [Online]. Available: https://www.c-and-a.jp/

[14] *Brillance Scintillators Performance Summary*, Saint-Gobain, Courbevoie, France, Jan. 2009. [Online]. Available: https://www.gammadata.se/assets/Uploads/SGC-BrilLanCe-Scintillators-Performance-Summary2.pdf

[15] "Shin-Etsu chemical." Accessed: Sep. 2022. [Online]. Available: https://www.shinetsu.co.jp/en

[16] "8×8 ch array, pixel pitch: 50 μm, with connector," Data Sheet MPPC S13361-3050AE-08, Hamamatsu, Shizuoka, Japan, May 2022. [Online]. Available: https://www.hamamatsu.com/content/dam/hamamatsu-photonics/sites/documents/99_SALES_LIBRARY/ssd/13361-3050_series_kapd1054e.pdf

[17] "Hamamatsu photonics." Accessed: Sep. 2022. [Online]. Available: https://www.hamamatsu.com/eu/en.html

[18] "Data sheet H8500C PMT," Data Sheet, Hamamatsu, Shizuoka, Japan. Accessed: 2022. [Online]. Available: https://www.hamamatsu.com/eu/en/product/type/H8500C/index.html

[19] S. Liprandi et al., "Characterization of a Compton camera setup with monolithic LaBr$_3$(Ce) absorber and segmented GAGG scatter detectors," in *Proc. IEEE NSS-MIC Conf.*, vol. 3, 2017, pp. 1–4.

[20] S. Takyu et al., "GAGG–MPPC detector with optimized light guide thickness for combined Compton-PET applications," *Nucl. Instrum. Methods Phys. Res. Sect. A, Accelerators Spectrometers Detectors Assoc. Equip.*, vol. 990, Feb. 2021, Art. no. 164998.

[21] S. Takyu et al., "Development of a DOI-based Compton camera for nuclear medicine application," in *Proc. IEEE NSS-MIC Conf. Poster*, 2017, p. 1.

[22] "Readout methods for arrays of silicon photomultipliers, rev. 3," Application Note AND9778/D, Semicond. Compon. Ind., LLC, Phoenix, AZ, USA, Sep. 2018.

[23] S. Aldawood et al., "Comparative characterization study of a LaBr$_3$(Ce) scintillation crystal in two surface wrapping scenarios: Absorptive and reflective," *Front. Oncol.*, vol. 5, p. 270, Dec. 2015.

[24] "Data sheet BC-630 silicone grease," Data Sheet, Saint-Gobain, Hiram, OH, USA, 2013. [Online]. Available: https://www.phenix.bnl.gov/WWW/ublish/bickleya/060622_RxnPSafety/MSDS_BC-630.pdf

[25] H. T. Van Dam et al., "Improved nearest neighbor methods for gamma photon interaction position determination in monolithic scintillator PET detectors," *IEEE Trans. Nucl. Sci.*, vol. 58, no. 5, pp. 2139–2147, Oct. 2011.

[26] A. Miani, "Determination of the spatial resolution of a monolithic scintillator in a Compton camera system with MeV range photons," M.S. thesis, Med. Phys. Dept., LMU Munich, Munich, Germany, 2016.

[27] "16 channel CFD with fast amplifier and pattern processing," Data Sheet MCFD-16 module, Mesytec GmbH, Putzbrunn, Germany. Accessed: 2022. [Online]. Available: http://www.mesytec.com/products/datasheets/MCFD-16.pdf

[28] "Fast 32 channel VME charge integrating ADC," Data Sheet MQDC-32 module, Mesytec GmbH, Putzbrunn, Germany. Accessed: 2022. [Online]. Available: http://www.mesytec.com/products/datasheets/MQDC-32.pdf

[29] "Data sheet quad coincidence logic unit—Mod. N455," Data Sheet, Caen, Viareggio, Italy. Accessed: 2022. [Online]. Available: https://www.caen.it/products/n455/

[30] "Data sheet quad logic fan-in/fan-out—Mod. 429A," Data Sheet, Teledyne LeCroy, Chestnut Ridge, NY, USA. Accessed: 2022. [Online]. Available: https://teledynelecroy.com/lrs/dsheets/428.htm

[31] J. Hoffmann, N. Kurz, and M. Richter. "TRIVA 5, VME trigger module." 2009. [Online]. Available: https://www.gsi.de/fileadmin/EE/Module/TRIVA/triva5f g5.pdf

[32] "RIO 3 power PC." GSI. Accessed: Sep. 2022. [Online]. Available: https://www.gsi.de/work/

[33] R. Lutter, O. Schaile, K. Schoffel, K. Steinberger, P. Thirolf, and C. Broude, "MAR/sub a/BOOU—A MBS and ROOT based online/offline utility," *IEEE Trans. Nucl. Sci.*, vol. 47, no. 2, pp. 280–283, Apr. 2000.

[34] A. Zoglauer, R. Andritschke, and F. Schopper, "MEGAlib—The medium energy gamma-ray astronomy library," *New Astron. Rev.*, vol. 50, pp. 629–632, Oct. 2006.

[35] S. J. Wilderman, N. H. Clinthorne, J. A. Fessler, and W. L. Rogers, "List-mode maximum likelihood reconstruction of Compton scatter camera images in nuclear medicine," in *Proc. Nucl. Sci. Symp. Conf. Rec.*, vol. 3, 1998, pp. 1716–1720.

[36] Y. Toko, N. Aoyama, K. Watanabe, K. Sakamori, and K. Endo, "Experimental study of a Si/CdTe semiconductor Compton camera for the next generation of gamma-ray astronomy," Ph.D. dissertation, Dept. Phys., Univ. Tokyo, Tokyo, Japan, 2008.

[37] S. Liprandi et al., "Sub-3mm spatial resolution from a large monolithic LaBr$_3$(Ce) scintillator," *Current Directions Biomed. Eng.*, vol. 3, no. 2, pp. 655–659, 2017.